PAPER

Strain effect in Pd@PdAg twinned nanocrystals towards ethanol oxidation electrocatalysis†

Jingbo Huang,[a] Qixing Liu,[a] Yucong Yan,[ac] Ningkang Qian,[a] Xingqiao Wu,[a] Liang Ji,[a] Xiao Li,[a] Junjie Li,[a] Deren Yang[a] and Hui Zhang ![ORCID] *[ab]

The strain effect is a critical knob to tune the catalytic performance and has received unprecedented research interest recently. However, it is difficult to distinguish the strain effect from the synergistic effect, especially in alloyed catalysts. Here we have synthesized Pd@PdAg icosahedra and {111} truncated bi-pyramids with only different surface strains between them as electrocatalysts for the ethanol oxidation reaction (EOR). Due to the same exposed facets and compositions of the two electrocatalysts, their EOR performances are mainly determined by the surface strains of PdAg alloys. These two electrocatalysts provide a perfect model to investigate the role of the strain effect in tuning the EOR performance. It is indicated that Pd@PdAg {111} truncated bi-pyramids with a surface strain of 0.3% show better catalytic activity and durability than Pd@PdAg icosahedra with a surface strain of 2.1% including commercial Pd/C. Density functional theory (DFT) calculations reveal that the lowered d-band center of 0.3% strained PdAg alloys relative to 2.1% strained ones reduced the adsorption energy of the acetate-evolution key intermediate $*CH_3CO$, thereby promoting the enhancement in the catalytic performance of Pd@PdAg nanocrystals for the EOR. Electrochemical analysis further verifies this demonstration on the key role of the strain effect in PdAg alloys for tuning catalytic performance.

Introduction

Direct ethanol fuel cells (DEFCs) are electrochemical energy conversion devices relying on the electrooxidation of ethanol. Due to the high energy density, high energy conversion efficiency, and non-toxicity of ethanol, DEFCs have spurred researchers to commercialize their applications in portable electronics and electric vehicles.[1–3] However, the commercialization of DEFCs has yet faced a series of difficulties, the most important one of which is the lack of electrocatalysts with high activity and long stability.[2–4] Pd-based nanocrystals are usually recognized as the most primary electrocatalysts towards the ethanol oxidation reaction (EOR) in alkaline solution.[5–7] Nevertheless, insufficient activity and unsatisfactory stability restrict the use of Pd in DEFCs. Since the poor durability arises from the poisoning of active sites on the surface of Pd by carbonaceous intermediates, alloying Pd with a second component such as Cu, Ag, Sn, Pb, *etc.* has been proposed as

a versatile strategy.[8–11] The introduction of a second metal can bring a well-known synergic effect, that is, the oxidation of ethanol occurs mainly on Pd atoms and the sites of other metals preferentially adsorb oxygen-containing species.[4,12,13] Therefore, carbonaceous intermediates can be oxidized and removed immediately by oxygen-containing species to enhance the activity and stability of Pd-based electrocatalysts.

Surface strain of nanocrystals is one of the most important factors that may influence their catalytic performance, and has drawn great attention in recent years. Engineering the surface strain of nanocrystals has proven to be an effective strategy to modify their electronic structures and regulate the adsorption energy of intermediates on the surface, thereby tuning the catalytic performance eventually.[14–16] For instance, Strasser *et al.* have reported that the d-band center of Pt with a thickness of five monolayers can be downshifted by 0.39 eV in the presence of only 2.5% compressive strain, which has dramatically altered the adsorption energy of the intermediate.[17] Huang *et al.* have demonstrated that the d-band center of Pd icosahedra with a tensile strain of 1.8% on the surface shifted upward from −1.46 to −1.40 eV, strengthening the adsorption of the key intermediate COOH*, and thus resulting in a higher faradaic efficiency for CO production.[18] Nowadays, strain engineering has become a widely used strategy to enhance the catalytic performance in many important reactions, such as the oxygen reduction reaction (ORR),[19,20] formic acid oxidation reaction (FAOR),[21] CO_2 reduction reaction (CO_2RR),[18,22] and nanozyme

[a]State Key Laboratory of Silicon Materials and School of Materials Science and Engineering, Zhejiang University, Hangzhou, Zhejiang 310027, People's Republic of China. E-mail: msezhanghui@zju.edu.cn

[b]Institute of Advanced Semiconductors, Hangzhou Innovation Center, Zhejiang University, Hangzhou, Zhejiang 310027, People's Republic of China

[c]BTR New Material Group CO., Ltd, GuangMing District, Shenzhen 518106, People's Republic of China

catalysis.[23] However, major research on the strain effect mentioned above focuses on a single metal (*e.g.*, Pd, Pt, Cu). Understanding the role of the strain effect in alloys has rarely been reported since it is difficult to distinguish the strain effect from the synergistic effect of alloys.

In this work, we investigate the role of the strain effect in Pd@PdAg twinned nanocrystals for tuning the EOR performance. Pd@PdAg icosahedra and {111} truncated bi-pyramids with different surface strains on PdAg alloys were synthesized through an interdiffusion method using Pd nanocrystals as templates. Pd@PdAg {111} truncated bi-pyramids with a surface strain of 0.3% showed prominently enhanced performance for the EOR compared to Pd@PdAg icosahedra with a surface strain of 2.1%. Density functional theory (DFT) calculations reveal that the lowered d-band center of 0.3% strained bi-pyramids weakened the adsorption of the acetate-evolution key intermediate *CH_3CO, and thus enhanced their catalytic performance towards the EOR compared to 2.1% strained icosahedra.

Results and discussion

To distinguish the strain effect from the synergistic effect of PdAg, two kinds of nanocrystals with the same facets and compositions, but different surface strains are needed to exclude the role of the facet and ligand effects. For this purpose, Pd icosahedra and {111} truncated bi-pyramids were firstly synthesized by the reduction of Na_2PdCl_4 in ethanol glycol (EG) through our previously reported methods (see ESI† for details).[24] Fig. S1 and S2† show morphological and structural characterization of Pd {111} truncated bi-pyramids and icosahedra, respectively. From TEM and HRTEM images in Fig. S1a–d,† we have successfully prepared Pd truncated bi-pyramids with {111} facets exposed on all the surfaces, which are definitely different from traditional Pd bi-pyramids (right bipyramids) with {100} exposed facets.[25] There are two typical projection profiles for the truncated bi-pyramids like the two models in Fig. S1c and d,† which are supported by the corresponding HRTEM images. In addition, a single twinned boundary is clearly observed in a truncated bi-pyramid (Fig. S1c†), indicating the formation of a single twinned nanocrystal. The interplanar spacings of 2.24–2.25 Å can be indexed to standard Pd {111} facets with negligible strain. The size of the short side and long side of Pd {111} truncated bi-pyramids was measured to be 11.7 ± 1.2 nm and 20.6 ± 2.3 nm, as shown in Fig. S1e.† The XRD pattern in Fig. S1f† further confirms the formation of negligible strained Pd nanocrystals since there is no obvious shift of the location of the {111} peak compared to the standard face-centered cubic (*fcc*) Pd. The TEM and HRTEM images in Fig. S2a and b† indicate the formation of Pd icosahedra with five-fold twined boundaries and {111} exposed facets. According to previous results,[26,27] {111} facets parallel to twinned boundaries around the surface of Pd icosahedra are dominated by the tensile strain, which is supported by the larger interplanar spacing of 2.31 Å in Fig. S2b† and the broadened {111} peak with a 0.4° shift to a low angle in Fig. S2d† compared to the standard one. The size of Pd icosahedra was measured to be 18.3 ± 1.3 nm, as shown in Fig. S2c.† These two kinds of Pd nanocrystals were then transferred into

OAm to serve as the starting materials for the construction of PdAg binary nanocrystals with different strains.

The Pd@PdAg nanocrystals were synthesized by diffusion of Ag atoms into Pd {111} truncated bi-pyramid and icosahedra, respectively, using our reported method.[24,28] Fig. 1 shows morphological, structural, and compositional characterization of the Pd@PdAg {111} truncated bi-pyramids. From the TEM (Fig. 1a and Fig. S3a†) and HRTEM (Fig. 1b) images, the products maintained the shape of {111} truncated bi-pyramids. The size of the short side of the bi-pyramids was measured to be 12.1 ± 1.2 nm, while the size of the long side reached 21.0 ± 2.3 nm (Fig. S3b†), suggesting a little volume expansion compared to Pd seeds because of the incorporation of Ag atoms. The interplanar spacing in the central area of the nanocrystals is 2.25 Å, which is equal to those of {111} facets of unstrained Pd. As for interplanar spacings of {111} planes near the surface, we measured the total distance of 10 groups of successive {111} planes. This value was then divided by 10 to reduce the measurement error. We analyzed two areas near the surface marked in Fig. 1b and the results are shown in Fig. 1c. The
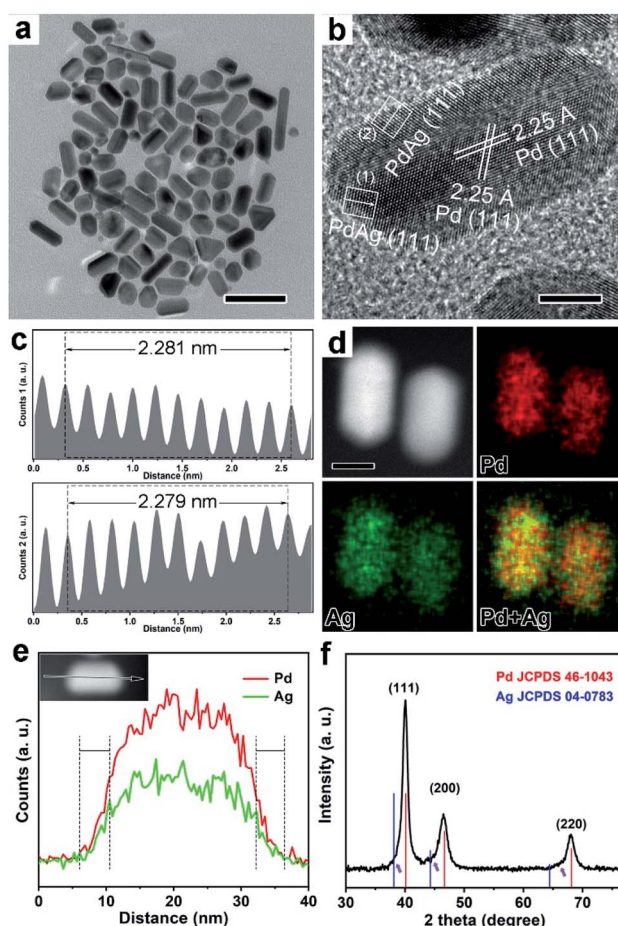

Fig. 1 Morphological, structural, and compositional characterization of the Pd@PdAg {111} truncated bi-pyramids nanocrystals. (a) TEM image, scale bar is 50 nm, (b) HRTEM image, scale bar is 5 nm, (c) intensity profiles recorded from the corresponding areas marked by rectangular boxes in (b). (d) EDX-mapping image, scale bar is 10 nm, (e) EDX line-scan analysis, and (f) XRD pattern.

interplanar spacings of the {111} planes of these two areas were 2.281 Å and 2.279 Å, respectively, which correspond to the lattices of PdAg alloys. From the EDX mapping image (Fig. 1d), the signal of the Ag element is a little stronger relative to that of Pd on the surface of the nanocrystals, while the interior of the nanocrystals is dominated by Pd. This demonstration is supported by EDX line-scan spectra (Fig. 1e). Fig. 1f shows the XRD pattern of the products prepared by diffusing Ag into Pd truncated bi-pyramids. As observed, three most intense peaks can be exactly indexed to standard Pd and each of them accompanies a small broadened peak on their left (marked with a purple arrow), indicating the coexistence of pure Pd and a little PdAg alloy. Taken together, the interior of the nanocrystals is composed of Pd, while the surface of the nanocrystals is dominated by PdAg alloys, indicating the formation of the Pd@PdAg core–shell structure. The atomic ratio of Ag is 7.8% as quantitatively determined by ICP-AES analysis.

To tune the size of the strain, Pd icosahedra with multiple twins were selected as the starting materials for the synthesis of

Pd@PdAg icosahedra, as shown in Fig. 2. After the diffusion of Ag, the nanocrystals also maintained the icosahedral shape (Fig. 2a, b and Fig. S4a†). From the statistics of the size (Fig.-S4b†), the distance of the face to face is largened a little and reaches 18.7 ± 0.9 nm. Similar to Pd@PdAg truncated bi-pyramids, the interplanar spacing in the interior of the icosahedra was 2.25 Å corresponding to the {111} facets of pure Pd, as shown in Fig. 2b (HRTEM image). The average lattice spacings of {111} facets on the surface of the icosahedra increased to 2.321 Å, a little bigger than the strained {111} facets of Pd icosahedra (*i.e.*, 2.31 Å) possibly due to the incorporation of Ag. The EDX mapping image (Fig. 2d) and line-scan profiles (Fig. 2e) show that Ag and Pd coexist near the surface of the icosahedra while the interior is dominated by Pd. This result indicates the formation of Pd@PdAg nanocrystals with a core–shell structure. From the XRD pattern in Fig. 2f, all the diffraction peaks were located between those of standard *fcc* Pd and *fcc* Ag, and shifted to a lower angle compared to those of standard *fcc* Pd, indicating the formation of PdAg alloys. We compared the shift degree of the {111} diffraction peak in Pd@PdAg icosahedra with standard *fcc* Pd and Pd icosahedra, as shown in the inset of Fig. 2f. As observed, there is 0.6° and 0.2° negative shift compared to {111} diffraction peaks of standard *fcc* Pd and Pd icosahedra, respectively. The atomic ratio of Ag is measured to be 8.0% by the ICP-AES technique, which is very close to that of Pd@PdAg {111} truncated bi-pyramids. It's worth noting that our previous work revealed an unexpected Kirkendall effect between Pd icosahedra and as deposited Cu or Ag atoms, leading to the formation of holes in the nanoparticles.[24] However, the amount of Ag precursor here was so little that enough vacancies did not form through interdiffusion of Ag and Pd atoms. The solid nanocrystals instead of hollow structures were eventually generated, which is consistent with our previous result.[24]

We aim to construct an ideal model to understand strain effects on PdAg alloys towards electrocatalysis using Pd@PdAg {111} truncated bi-pyramids and icosahedra as electrocatalysts. Therefore, we try to keep other variable factors that influence the electrocatalysis performance the same. Since two kinds of samples were synthesized in the same solvent using the same reagents (*i.e.*, PVP, KBr, AA, Na_2PdCl_4), the surface state is supposed to be the same. Considering that both nanocrystals are bounded by {111} facets, the facet effect could be ruled out. We could also ignore the size effect due to the similar sizes of Pd@PdAg truncated bi-pyramids and icosahedra. Based on ICP-AES tests, the atomic ratios of Ag in the whole nanocrystals of the two samples were similar (7.8% *vs.* 8.0%). But the surface composition is more critical to determine the electrocatalytic performance.[29] As such, we quantified the atomic ratio of Ag on the surface of these two samples through XPS analyses. It is indicated that the atomic ratios of Ag are 24.5% and 25.1% for {111} truncated bi-pyramids and icosahedra, respectively, excluding the influence of surface composition on the performance. In addition, the electron transfer between Pd and Ag in these two samples was investigated by XPS as shown in Fig. 3. All the peaks associated with Ag and Pd can be split into two peaks, suggesting the presence of two valence states (*i.e.*, metal
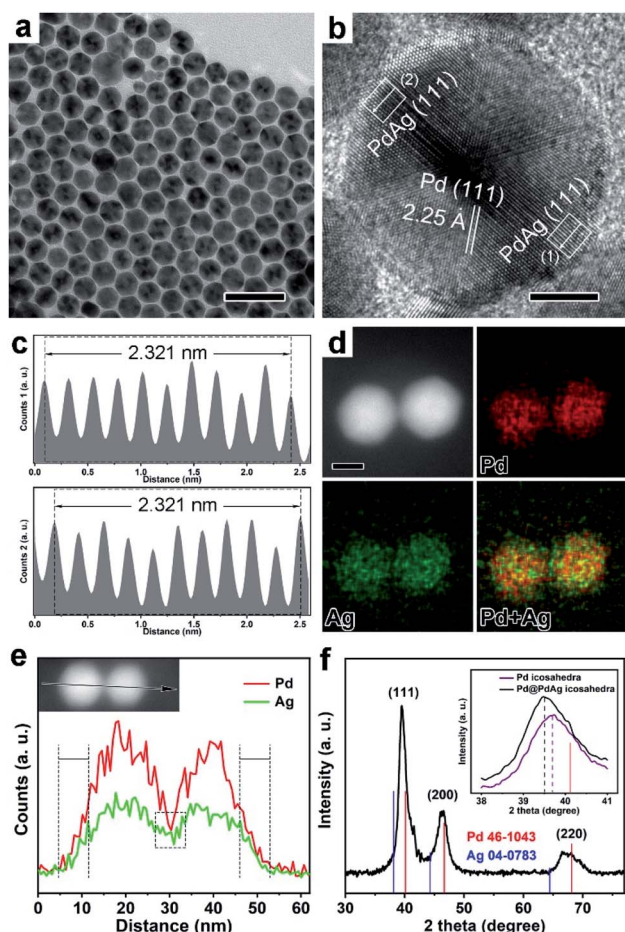

Fig. 2 Morphological, structural, and compositional characterization of the Pd@PdAg icosahedra nanocrystals. (a) TEM image, scale bar is 50 nm, (b) HRTEM image, scale bar is 5 nm, (c) intensity profiles recorded from the corresponding areas marked by rectangular boxes in (b). (d) EDX-mapping image, scale bar is 10 nm, (e) EDX line-scan analysis, and (f) XRD pattern. Inset in (f) shows the contrast of {111} peaks of Pd@PdAg icosahedra and Pd icosahedra nanocrystals.
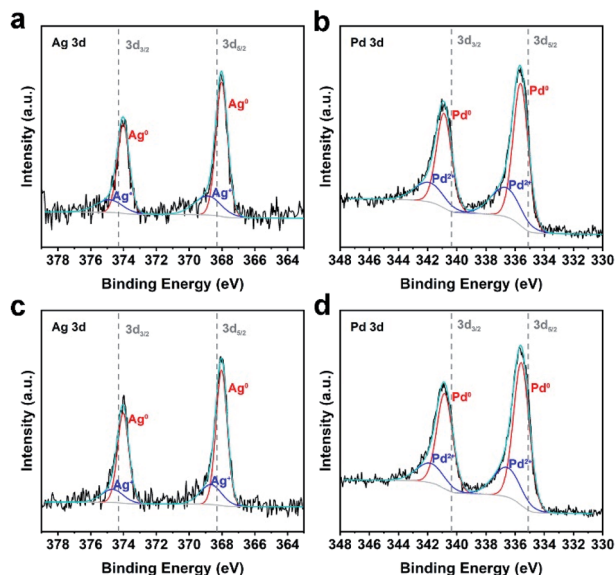
Fig. 3 High-resolution XPS spectra of (a and b) Pd@PdAg {111} truncated bi-pyramids and (c and d) Pd@PdAg icosahedra nanocrystals. (a and c) Ag 3d and (b and d) Pd 3d XPS spectra. The peaks were split to reflect different contributions.
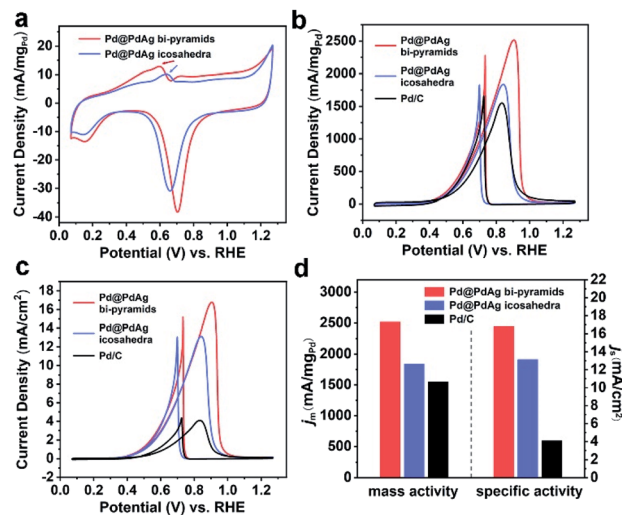

Fig. 4 Electrochemical measurements of Pd@PdAg nanocrystals for the EOR. (a) CV curves of carbon-loaded Pd@PdAg nanocrystals in 1 M KOH solution normalized to the mass of Pd, (b and c) CV curves of carbon-loaded Pd@PdAg nanocrystals and commercial Pd/C in 1 M KOH solution containing 1 M ethanol normalized to the mass of Pd (b) and the ECSAs (c). (d) Mass and specific activities of carbon-loaded Pd@PdAg nanocrystals including commercial Pd/C at a peak potential.

and oxidation state). As shown in Fig. 3a and c, the peaks of Ag^0 $3d_{5/2}$ and $3d_{3/2}$ shifted to lower energy with respect to standard Ag^0. Conversely, the peaks of Pd^0 $3d_{5/2}$ and $3d_{3/2}$ shifted to higher energy with respect to standard Pd^0 (Fig. 3b and d), indicating electron transfer from Pd to Ag atoms. The difference in the shift of the binding energy for Pd^0 in the two samples relative to standard Pd^0 (Fig. 3b and d) is negligible, indicating a similar electron coupling effect (i.e., ligand effect) for Pd@PdAg {111} truncated bi-pyramids and icosahedra. The size of strain is different for these two samples due to the different amounts of twins existing in the nanocrystals. Therefore, the main difference between the two Pd-based electrocatalysts is the variation of surface strain in the PdAg alloys (i.e., strain effect), which is a dominant factor towards ethanol oxidation.

The Pd@PdAg {111} truncated bi-pyramids and icosahedra were loaded uniformly onto a Vulcan XC-72R carbon black support (Fig. S5a and b†) and subsequently were evaluated as electrocatalysts towards the ethanol oxidation reaction (EOR). We chose commercial Pd/C as a contrast sample (Fig. S5c†). The CV curves of these three catalysts were recorded at room temperature in Ar-saturated 1 M KOH solutions at a sweep rate of 50 mV s^{-1} between 0.07 and 1.27 V versus RHE. The CV curves of the carbon-loaded Pd@PdAg catalysts are shown in Fig. 4a, and the one of Pd/C is shown in Fig. S6.† The pronounced peak between 0.9 and 0.5 V during the negative sweep in each CV curve can be attributed to the reduction of surface Pd(II) oxide.[30,31] The ECSA of each catalyst was calculated by measuring the charge transfer in the oxidation of monolayer CO adsorbed on the metal surface via the CO stripping method (Fig. S7†). The ECSAs of carbon-loaded Pd@PdAg {111} truncated bi-pyramids, icosahedra, and Pd/C are 15.0, 14.0, and 37.9 m^2 g$^{-1}_{Pd}$, respectively. To evaluate the EOR activity of these

catalysts, CV was recorded in Ar-saturated solution containing 1 M KOH and 1 M ethanol at a sweep rate of 50 mV s^{-1} between 0.07 and 1.27 V versus RHE. Since the activity towards the EOR was mostly contributed by Pd sites, we normalized the current of CV curves with respect to the mass of Pd, as shown in Fig. 4b.[9] Carbon-loaded Pd@PdAg {111} truncated bi-pyramids exhibited a much higher mass current density (2517 mA mg$^{-1}_{Pd}$), substantially larger than those of carbon-loaded Pd@PdAg icosahedra (1838 mA mg$^{-1}_{Pd}$) and Pd/C (1551 mA mg$^{-1}_{Pd}$). We also evaluated the intrinsic activities of the three Pd-based catalysts through normalizing CV curves by ECSAs (Fig. 4c). The specific activity of carbon-loaded Pd@PdAg {111} truncated bi-pyramids (16.8 mA cm^{-2}) for the EOR is still superior to those of carbon-loaded Pd@PdAg icosahedra (13.1 mA cm^{-2}) and Pd/ C (4.1 mA cm^{-2}). The largest values of mass activity and specific activity of the three catalysts are displayed in Fig. 4d. The cycling stabilities of such three catalysts were studied by continuously performing CV cycles at the sweep rate of 50 mV s^{-1} between 0.07 and 1.27 V. Fig. S8† displays the mass activities of the catalysts against the cycle numbers, from which it is found that their mass activities decreased gradually during the cycling. The mass activity of carbon-loaded Pd@PdAg {111} truncated bi-pyramids remained at 714 mA mg$^{-1}_{Pd}$ after 1000 cycles, which is still 1.3 times higher than that of Pd@PdAg icosahedra (551 mA mg$^{-1}_{Pd}$) and 6.5 times higher than that of Pd/C (110 mA mg$^{-1}_{Pd}$). These experimental results undoubtedly reveal that the catalytic performance of carbon-loaded Pd@PdAg {111} truncated bi-pyramids towards the EOR is much higher than that of carbon-loaded Pd@PdAg icosahedra. Moreover, since the surface atomic ratio of Ag is 24.5% for Pd@PdAg {111} truncated bi-pyramids (approximately labelled as Pd@Pd$_3$Ag), the mass activities of carbon-loaded Pd@Pd$_{1.3}$Ag and Pd {111}

truncated bi-pyramids were also measured for comparison, as shown in Fig. S9.† As observed, Pd@Pd$_3$Ag possesses much enhanced mass activity compared to Pd@Pd$_{1.3}$Ag and pure Pd. As such, the introduction of Ag can promote the enhancement in EOR activity by tuning the d-band center of Pd. However, the excess of Ag can block the Pd active sites, and thus deteriorate the EOR performance.[10]

To intrinsically understand the strain effect of Pd@PdAg nanocrystals on the EOR, we performed DFT calculation to determine the position of the d-band center and adsorption energy of the intermediate on the catalysts. Firstly, we calculated the values of surface strain of these two types of nanocrystals. According to Vegard's law, the crystal cell parameter of an alloy is linearly related to its composition.[32] Since the surface atomic ratios of Ag are 24.5% and 25.1% for {111} truncated bi-pyramids and icosahedra, respectively, we chose an approximate value of 25% (*i.e.*, Pd$_3$Ag) to calculate the standard interplanar spacings of {111} facets (*i.e.*, 2.274 Å). Using interplanar spacings on the surface of the nanocrystals measured previously in Fig. 1c and 2c, the strains of Pd$_3$Ag alloys for Pd@PdAg {111} truncated bi-pyramids and icosahedra are calculated to be 0.3% and 2.1%, respectively.[17] After that, we built three models of Pd$_3$Ag (111) planes with strains of 0.3% and 2.1% and ideal Pd (111) planes (Fig. S10†) to calculate the electronic band structures, as shown in Fig. 5a. The d-band centers (with regard to the Fermi level) of Pd$_3$Ag (111) planes with strains of 0.3% and 2.1% and ideal Pd (111) planes are −2.37, −2.18, and −2.02 eV, respectively. With the incorporation of Ag atoms, the d-band center of Pd (111) shifted downwards prominently. However, as for Pd$_3$Ag (111) planes, tensile strain can induce an upward shift of the d-band center (*i.e.*, from −2.37 eV of 0.3% to −2.18 eV of 2.1%), which is similar to the trend of Pd octahedra and icosahedra.[18] According to Nørskov *et al.*,[33] the higher the d states (*i.e.*, the d-band center) with respect to the Fermi level, the higher the antibonding state energy and the stronger the adsorbate bonding. Hence the weaker the tensile strain on the Pd$_3$Ag (111) planes, the weaker the adsorption energies of intermediates towards the EOR. Since the products of the EOR on the surface of the Pd-based catalysts are dominated by C$_2$ species, the oxidation of *CH$_3$CO by *OH to form acetate is the rate-determining step.[4,30] Therefore, the adsorption energy of *CH$_3$CO on the catalysts is a critical descriptor of the intrinsic activity for the EOR to acetate. The weaker the adsorption energy (*i.e.*, a less negative adsorption energy) of *CH$_3$CO, the easier the oxidation of *CH$_3$CO to acetate. We used the aforementioned three models to calculate the adsorption energies of *CH$_3$CO, as shown in Fig. 5b. In accordance with the result of d-band centers, the adsorption energies of *CH$_3$CO on these three models followed a sequence of ideal Pd (111) < 2.1% strained Pd$_3$Ag (111) < 0.3% strained Pd$_3$Ag (111), suggesting that Pd$_3$Ag (111) planes with a strain of 0.3% are more active than the structure with a strain of 2.1% than Pd (111). As such, Pd@PdAg {111} truncated bi-pyramids show the best catalytic performance towards the EOR.

The best EOR performance of Pd@PdAg {111} truncated bi-pyramids can be further understood through electrochemical analysis. Since the adsorbed intermediates *CH$_3$CO can be oxidized by *OH to acetate, the adsorption potential of *OH is rather important to the performance towards the EOR.[30] The CV curves of the two types of Pd@PdAg nanocrystals are shown in Fig. 4a, and the peaks marked by arrows correspond to the adsorption of *OH.[34,35] As can be seen, the peak potential of Pd@PdAg {111} truncated bi-pyramids was around 0.6 V *vs.* RHE, which was 0.04 V lower than that of Pd@PdAg icosahedra (0.64 V *vs.* RHE), indicating easier adsorption of *OH and oxidation of *CH$_3$CO on the surface of Pd@PdAg {111} truncated bi-pyramids. Since the adsorbed intermediates *CO on active sites generated from the cleavage of C–C bonds can poison the catalysts and thus deteriorate the stability, we analyzed the CO-stripping curves of Pd@PdAg nanocrystals. From Fig. S7b,† compared to a broad CO-oxidation peak located around 1.02 V *vs.* RHE for Pd@PdAg icosahedra, Pd@PdAg {111} truncated bi-pyramids have a sharp peak around 0.79 V together with a shoulder peak around 1.0 V. A small CO-oxidation peak can still be observed after CO-stripping for Pd@PdAg icosahedra, indicating that CO cannot be completely removed from the surface of Pd@PdAg icosahedra. However, the CO-oxidation peak disappeared in the second cycle of Pd@PdAg {111} truncated bi-pyramids. The negative shift of the CO-oxidation peak and complete oxidation of CO for Pd@PdAg {111} truncated bi-pyramids compared to Pd@PdAg icosahedra suggest easier oxidation of CO on the surface of truncated bi-pyramids, thus improving the capability of tolerance for CO poisoning and promoting the enhancement in EOR performance.[36]
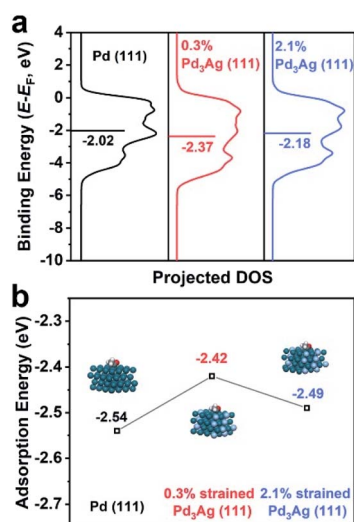
Conclusions

In summary, we have constructed an ideal platform to reveal the strain effect on the EOR by synthesizing Pd@PdAg icosahedra

Fig. 5 (a) Projected d-density of the states (PDOS) of the surface atoms of ideal Pd (111) and Pd$_3$Ag (111) with strains of 0.3% and 2.1%. The d-band centers are marked by horizontal lines. (b) Adsorption energies of *CH$_3$CO on ideal Pd (111) and Pd$_3$Ag (111) with strains of 0.3% and 2.1%.

and {111} truncated bi-pyramids with the same facets and compositions, but different surface strains. Pd@PdAg {111} truncated bi-pyramids with a surface strain of 0.3% exhibited remarkably enhanced mass activity and stability for the EOR relative to Pd@PdAg icosahedra with a surface strain of 2.1% and Pd/C. DFT calculations suggested that the d-band center of 0.3% strained PdAg alloys was a little lower than that of 2.1% strained PdAg alloys, which weakened the adsorption of the acetate-evolution intermediate *CH$_3$CO, and thus enhanced the catalytic performance towards the EOR. Such enhancement was further understood by electrochemical analysis including CV and CO striping measurements. Our findings provide a deep understanding of the strain effect solely towards electrocatalysis, and can be extended to the design of other advanced catalysts with excellent performance for important reactions in fine chemical production, energy conversion, and environmental protection.

Conflicts of interest

The authors declare that they have no conflict of interest.

Acknowledgements

References

1 M. Z. F. Kamarudin, S. K. Kamarudin, M. S. Masdar and W. R. W. Daud, *Int. J. Hydrogen Energy*, 2013, **38**, 9438–9453.

2 M. A. F. Akhairi and S. K. Kamarudin, *Int. J. Hydrogen Energy*, 2016, **41**, 4214–4228.

3 E. Antolini, *J. Power Sources*, 2007, **170**, 1–12.

4 J. Bai, D. Liu, J. Yang and Y. Chen, *ChemSusChem*, 2019, **12**, 2117–2132.

5 C. Bianchini and P. Shen, *Chem. Rev.*, 2009, **109**, 4183–4206.

6 L. Zhang, Q. Chang, H. Chen and M. Shao, *Nano Energy*, 2016, **29**, 198–219.

7 Y.-Y. Yang, J. Ren, Q.-X. Li, Z.-Y. Zhou, S.-G. Sun and W.-B. Cai, *ACS Catal.*, 2014, **4**, 798–803.

8 X. Zhao, L. Dai, Q. Qin, F. Pei, C. Hu and N. Zheng, *Small*, 2017, **13**, 1602970.

9 W. Huang, X. Kang, C. Xu, J. Zhou, J. Deng, Y. Li and S. Cheng, *Adv. Mater.*, 2018, **30**, 1706962.

10 H. Lv, Y. Wang, A. Lopes, D. Xu and B. Liu, *Appl. Catal., B*, 2019, **249**, 116–125.

11 Q. Gao, T. Mou, S. Liu, G. Johnson, X. Han, Z. Yan, M. Ji, Q. He, S. Zhang, H. Xin and H. Zhu, *J. Mater. Chem. A*, 2020, **8**, 20931–20938.

12 E. Antolini, *Energy Environ. Sci.*, 2009, **2**, 915–931.

13 Z. Zhang, J. Liu, J. Gu, L. Su and L. Cheng, *Energy Environ. Sci.*, 2014, **7**, 2535–2558.

14 M. E. Escribano, P. Malacrida, M. H. Hansen, U. G. V. Hansen, A. V. Palenzuela, V. Tripkovic, J. Schiøtz, J. Rossmeisl, I. E. L. Stephens and I. Chorkendorff, *Science*, 2016, **352**, 73–76.

15 H. Wang, S. Xu, C. Tsai, Y. Li, C. Liu, J. Zhao, Y. Liu, H. Yuan, F. A. Pedersen, F. B. Prinz, J. K. Nørskov and Y. Cui, *Science*, 2016, **354**, 1031–1036.

16 L. Wang, Z. Zeng, W. Gao, T. Maxson, D. Raciti, M. Giroux, X. Pan, C. Wang and J. Greeley, *Science*, 2019, **363**, 870–874.

17 P. Strasser, S. Koh, T. Anniyev, J. Greeley, K. More, C. Yu, Z. Liu, S. Kaya, D. Nordlund, H. Ogasawara, M. F. Toney and A. Nilsson, *Nat. Chem.*, 2010, **2**, 454–460.

18 H. Huang, H. Jia, Z. Liu, P. Gao, J. Zhao, Z. Luo, J. Yang and J. Zeng, *Angew. Chem., Int. Ed.*, 2017, **56**, 3594–3598.

19 J. X. Wang, C. Ma, Y. Choi, D. Su, Y. Zhu, P. Liu, R. Si, M. B. Vukmirovic, Y. Zhang and R. R. Adzic, *J. Am. Chem. Soc.*, 2011, **133**, 13551–13557.

20 Y. Xiong, H. Shan, Z. Zhou, Y. Yan, W. Chen, Y. Yang, Y. Liu, H. Tian, J. Wu, H. Zhang and D. Yang, *Small*, 2017, **13**, 1603423.

21 S. I. Choi, J. A. Herron, J. Scaranto, H. Huang, Y. Wang, X. Xia, T. Lv, J. Park, H. C. Peng, M. Mavrikakis and Y. Xia, *ChemCatChem*, 2015, **7**, 2077–2084.

22 R. Reske, M. Duca, M. Oezaslan, K. J. P. Schouten, M. T. M. Koper and P. Strasser, *J. Phys. Chem. Lett.*, 2013, **4**, 2410–2413.

23 Z. Xi, X. Cheng, Z. Gao, M. Wang, T. Cai, M. Muzzio, E. Davidson, O. Chen, Y. Jung, S. Sun, Y. Xu and X. Xia, *Nano Lett.*, 2020, **20**, 272–277.

24 J. Huang, Y. Yan, X. Li, X. Qiao, X. Wu, J. Li, R. Shen, D. Yang and H. Zhang, *Nano Res.*, 2020, **13**, 2641–2649.

25 Y. Xiong, H. Cai, Y. Yin and Y. Xia, *Chem. Phys. Lett.*, 2007, **440**, 273–278.

26 C. L. Johnson, E. Snoeck, M. Ezcurdia, B. R. González, I. P. Santos, L. M. L. Marzán and M. J. Hÿtch, *Nat. Mater.*, 2008, **7**, 120–124.

27 A. Howie and L. D. Marks, *Philos. Mag. A*, 1984, **49**, 95–109.

28 X. Li, X. Wang, M. Liu, H. Liu, Q. Chen, Y. Yin and M. Jin, *Nano Res.*, 2018, **11**, 780–790.

29 Z. W. Seh, J. Kibsgaard, C. F. Dickens, I. Chorkendorff, J. K. Nørskov and T. F. Jaramillo, *Science*, 2017, **355**, eaad4998.

30 Z. X. Liang, T. S. Zhao, J. B. Xu and L. D. Zhu, *Electrochim. Acta*, 2009, **54**, 2203–2208.

31 A. L. Wang, X. J. He, X. F. Lu, H. Xu, Y. X. Tong and G. R. Li, *Angew. Chem., Int. Ed.*, 2015, **54**, 3669–3673.

32 A. R. Denton and N. W. Ashcroft, *Phys. Rev. A*, 1991, **43**, 3161–3164.

33 J. K. Nørskov, F. A. Pedersen, F. Studt and T. Bligaard, *Proc. Natl. Acad. Sci. U.S.A.*, 2011, **108**, 937–943.

34 S. Zhang, P. Kang and T. J. Meyer, *J. Am. Chem. Soc.*, 2014, **136**, 1734–1737.

35 F. Lei, W. Liu, Y. Sun, J. Xu, K. Liu, L. Liang, T. Yao, B. Pan, S. Wei and Y. Xie, *Nat. Commun.*, 2016, **7**, 12697.

36 D. Gao, H. Zhou, J. Wang, S. Miao, F. Yang, G. Wang, J. Wang and X. Bao, *J. Am. Chem. Soc.*, 2015, **127**, 4288–4291.